Nonlinear Baroclinic Dynamics of Surface Cyclones Crossing a Zonal Jet

Jean-Baptiste Gilet, Matthieu Plu, Gwendal Rivière

Nonlinear Baroclinic Dynamics of Surface Cyclones Crossing a Zonal Jet

JEAN-BAPTISTE GILET

GAME/CNRM, Météo-France, CNRS, Toulouse, France

MATTHIEU PLU

GAME/CNRM, Météo-France, CNRS, Toulouse, and LACY, Unité Mixte CNRS–Météo-France–Université de La Réunion, Saint-Denis de la Réunion, France

GWENDAL RIVIÈRE

GAME/CNRM, Météo-France, CNRS, Toulouse, France

(Manuscript received 28 January 2009, in final form 27 April 2009)

ABSTRACT

Mechanisms leading a synoptic surface cyclone to cross an upper-level zonal jet and its subsequent deepening are investigated using a two-layer model on a β plane. The baroclinic interaction of a low-level circular cyclonic perturbation with an upper-level one is first studied in vertical and horizontal cyclonic or anticyclonic uniform shears. A first nonlinear effect acting on the shape and energetics of the perturbations is analyzed. If the background shear is anticyclonic, the perturbations are stretched horizontally; they lose energy barotropically but gain it baroclinically by a well-maintained westward tilt with height. Conversely, if the shear is cyclonic, perturbations remain quite isotropic, but they do not keep a favorable vertical tilt with time and the baroclinic interaction is thus only transient. The latitudinal motion of the perturbations also results from a nonlinear effect. It is found to depend strongly on the background potential vorticity (PV) gradient. This effect is a baroclinic equivalent of the so-called nonlinear barotropic "β drift" and combines the nonlinear advection and vertical stretching terms.

These results are confirmed when the anomalies are initially located south of a confined westerly jet. The poleward shift of the lower cyclonic anomaly occurs faster when the vertically averaged PV gradient is strongly positive, which happens when the jet has a large barotropic component. The lower anomaly crosses the jet from the warm to the cold side and deepens afterward. After a detailed description of this regeneration process with the help of an energy budget, it is shown that linear dynamics are not able to reproduce such behavior.

1. Introduction

Intense storms in the northeastern Atlantic Basin evolve following a variety of complex life cycles. An often observed cycle consists of an appearance in the southern part of an upper-level large-scale jet, eastward translation without significant amplification on this anticyclonic side, and then sudden and intense growth while the depression crosses the jet axis. The Christmas 1999 Lothar storm over Europe is one example (Rivière and Joly 2006b). Similar but less spectacular cyclone growth during jet crossing from the warm to the cold side was found fairly systematically during the Fronts and Atlantic Storm Track Experiment (FASTEX) campaign (Baehr et al. 1999). A detailed energy budget was drawn up for the case of intensive observing period (IOP) 17 by Rivière and Joly (2006a), from which it was found that both the barotropic and baroclinic interactions were decisive in the cyclone deepening. More precisely, during the crossing, the barotropic sink was temporarily stopped by a transient contraction of the cyclone horizontal structure and a new phase of baroclinic interaction occurred. The purpose of the present paper is to reproduce and analyze such a jet-crossing transition by a surface cyclone in very idealized numerical simulations.

As far as these evolutions are concerned, there is a clear lack of systematic idealized studies. Davies et al. (1991) made a detailed examination of the influence of a

Corresponding author address: Jean-Baptiste Gilet, Météo-France, CNRM/GMAP/RECYF, 42 Avenue G. Coriolis, 31057 Toulouse CEDEX, France.
E-mail: jean-baptiste.gilet@meteo.fr

DOI: 10.1175/2009JAS3086.1

horizontal shear on the structure of cyclones embedded in a zonal jet in a semigeostrophic model but did not explore the energy interactions or the dynamic mechanisms leading to the jet crossing. Sudden growth during the jet crossing is usually put down to the mechanism proposed by Uccelini (1990), which highlights the central role of the diffluent cold side exit region for cyclogenesis revival. As the present study tackles the crossing of purely zonal flows, the latter effect is discarded. More precisely, this paper aims to provide some insight into the shape variation, deepening, and trajectory of midlatitude cyclones embedded in jets that have both baroclinic and barotropic components on an f and a β plane. It also concentrates on finite-amplitude perturbations, so the genesis of depressions is beyond the scope of the present paper. In particular, we investigate which mechanisms lead to the jet crossing, how the observed sudden perturbation growth during the crossing can be explained, and what the respective roles of linear and nonlinear mechanisms are.

The stretching and change of orientation of idealized (circular or elliptical) structures by background shears is quite a standard result in the barotropic framework. Kida (1981) provided the rate of change of the isotropy and orientation of constant vorticity elliptical cyclones that evolve nonlinearly in basic flows having both strain and vorticity parts. Legras and Dritschel (1993) and Marcus et al. (2000) showed the differences induced by a change of sign of the ratio between environmental and vortex vorticity: whereas same-signed vortices hold up, opposite-signed ones fragment. Dritschel (1998) demonstrated that the initial profile of the cyclone is of prime importance both for the self-advection of a cyclone and especially for its orientation. In the present work, results on the shape evolution will be revisited and extended to a baroclinic two-layer atmosphere.

In the field of geophysical dynamics, the trajectories of tropical cyclones and oceanic lenses have been studied extensively, through idealized and more realistic numerical simulations and through observations. However, few investigations have given prominence to the factors influencing the trajectories of midlatitude cyclones in a baroclinic atmosphere.

As far as tropical cyclones are concerned, since the pioneering theoretical works of Rossby (1948) and Adem (1956), numerical experiments (Madala and Piacsek 1975; Holland 1983; Willoughby 1988; Smith and Ulrich 1990; Shapiro 1992, among many others) have shown that one of the basic motion components is the so-called β drift. Because of the existence of the planetary vorticity gradient due to the earth's roundness, a west–east vorticity dipole centered on the vortex is created, causing a westward propagation (this argument is linear and is therefore also true for anticyclones) and gives rise to poleward nonlinear advection of the parent cyclone. Moreover, when the cyclone's environment is not at rest, it has been noted that a tropical cyclone tends to move to the left and faster than the flow in which it evolves (Anthes 1982). Holland (1983) pointed out that this phenomenon was strongly influenced by the basic flow asymmetries. Shapiro (1992) refined these results by finding that in a three-layer baroclinic model with physical parameterization, the cyclone trajectory, the vorticity of which is mostly located in the lowest levels, is mainly controlled by the meridional isentropic gradient of background potential vorticity (PV) in the midlayer, through the same nonlinear mechanism as the classical β-drift scheme.

In the field of oceanic vortices, McWilliams and Flierl (1979) found evidence that the background PV gradient associated with both β and the basic flow is a key parameter in the analysis of the zonal and meridional components of the trajectory of finite-amplitude isolated vortices. Morel and McWilliams (1997) and Sutyrin and Morel (1997) showed that a change in the vortex vertical structure could lead to a large diversity of evolutions and thus different trajectories, through nonlinear interaction between upper and lower parts of the vortex and through the nonlinear action of the basic flow PV gradient. In summary, both tropical cyclones and oceanic vortices' trajectories have been proven to be controlled, if only partially, by background PV gradient, the effect of which is modulated by the structural details of the vortices.

In the field of synoptic midlatitude dynamical meteorology, it has long been observed that the trajectories of strong cyclones have a cross-jet component, pointing to the left of the jet in the Northern Hemisphere [see Wallace et al. (1988) and the subsequent comment by Alpert (1989)]. The nonlinear integrations of idealized quasigeostrophic (QG), semigeostrophic (SG), and primitive equation (PE) simulations on f planes, initialized with favorably vertically tilted vortices (Simmons and Hoskins 1978; Hoskins and West 1979; Schär and Wernli 1993; Takayabu 1991; Plu and Arbogast 2005) exhibit a quasi-systematic poleward (equatorward) shift of surface cyclones (anticyclones). Takayabu (1991) stressed the fact that the interaction with an upper disturbance is predominant in the mechanisms leading to the poleward displacement. It should be noted that Rivière (2008) studied the effects of jet crossing by synoptic-scale eddies in a barotropic framework and underlined the key role played by nonlinear dynamics.

There is therefore a clear need to revisit and explore more or less well-known results on geophysical fluids in the context of midlatitude depressions. Through highly idealized experiments, this paper aims to shed some light on the mechanisms leading to the evolution of the

energetics and trajectories of midlatitude synoptic disturbances. Section 2 reviews the models used and the methodology employed to isolate the mechanisms involved. In section 3, the evolution of the shape and intensity of vortices in uniform barotropic and mixed barotropic–baroclinic cyclonic and anticyclonic shears is studied. Section 4 emphasizes the effect of the basic-state PV gradient on the trajectories of cyclonic vortices. Section 5 synthesizes the mechanisms highlighted in the two preceding sections, with the help of a simulation of the evolution on an f plane of a vortex initially situated on the anticyclonic side of a confined jet.

2. Experimental framework

a. Model

The quasigeostrophic baroclinic two-layer model (Phillips 1951) was used. The horizontal domain is a two-dimensional biperiodic plane (x, y), oriented by the basis $(\mathbf{i}, \mathbf{j})$ such that $\mathbf{i}$ points to the east and $\mathbf{j}$ to the north. The domain is taken to be in the Northern Hemisphere, but the transposition of the results to the Southern Hemisphere is straightforward. The total flow is divided into a zonal and thus stationary basic state (denoted with an overbar) and a perturbation (denoted with primes) without any assumption about their amplitudes and the linearity of their evolutions. The model is spectral, the nonlinear terms are computed on a regular grid, and the temporal scheme is a leapfrog one.

The Phillips (1951) two-layer model is one of the simplest baroclinic models. It consists of the advection of potential vorticity q:

$$q_u = \Delta\psi_u + (f_0 + \beta y) - \lambda^{-2}(\psi_u - \psi_l), \tag{1}$$

$$q_l = \Delta\psi_l + (f_0 + \beta y) + \lambda^{-2}(\psi_u - \psi_l), \quad \text{and} \tag{2}$$

$$\frac{\partial q_k}{\partial t} + \mathbf{u_k} \cdot \nabla q_k = 0, \tag{3}$$

where $k \in \{u, l\}$ denotes the upper or the lower layer; $\mathbf{u_k} = (u_k, v_k)$ is the geostrophic wind; ψ_k is the streamfunction in the k layer; $f = f_0 + \beta y$ is the Coriolis parameter, with β being its latitudinal variation; and λ is the Rossby deformation radius. The values of the input parameters are given in Table 1. It is straightforward that when λ^{-2} is equal to 0, this model is reduced to a pair of nondivergent barotropic models.

TABLE 1. Input model parameters.

U	Horizontal velocity scale	48 m s^{-1}
H	Vertical length scale	4.5×10^3 m
α	Standard velocity shear	2.4×10^{-5} s^{-1}
f_0	Uniform Coriolis parameter	10^{-4} s^{-1}
β_0	β of reference	1.6×10^{-11} m^{-1} s^{-1}
λ	Rossby deformation radius	4.5×10^5 m

b. Diagnoses

1) VORTICITY TENDENCIES

Following Eq. (3), the evolution of the perturbation relative vorticity can be expressed as

$$\frac{\partial \zeta'_u}{\partial t} + \mathbf{u'_u} \cdot \nabla\overline{\zeta_u} + \overline{\mathbf{u_u}} \cdot \nabla\zeta'_u + \mathbf{u'_u} \cdot \nabla\zeta'_u - \beta v'_u = -f_0 \frac{w_m}{H}, \quad \text{and} \tag{4}$$

$$\frac{\partial \zeta'_l}{\partial t} + \mathbf{u'_l} \cdot \nabla\overline{\zeta_l} + \overline{\mathbf{u_l}} \cdot \nabla\zeta'_l + \mathbf{u'_l} \cdot \nabla\zeta'_l - \beta v'_u = +f_0 \frac{w_m}{H}, \tag{5}$$

where w_m is the vertical velocity at the interface between the two layers and H is the vertical distance between the midlevels of the layers.

The right-hand sides of Eqs. (4) and (5) can be split into linear and nonlinear contributions (see appendix for more details). This leads to the following decomposition:

$$\text{for } k \in \{u, l\}, \quad \frac{\partial \zeta'_k}{\partial t} = -(\mathbf{u'_k} \cdot \nabla\overline{\zeta_k} + \overline{\mathbf{u_k}} \cdot \nabla\zeta'_k) - \beta v'_k - (-1 + 2\delta_{k=l}) f_0 \frac{w_{m,\mathrm{LIN}}}{H} - \mathbf{u'_k} \cdot \nabla\zeta'_k - (-1 + 2\delta_{k=l}) f_0 \frac{w_{m,\mathrm{NL}}}{H}, \tag{6}$$

where δ_* is the Kronecker delta. The first three terms on the right-hand side are linear (the advection of relative and planetary vorticity and the linear vertical stretching) and the two last are nonlinear (self-advection of relative vorticity and nonlinear vertical stretching).

2) ENERGETICS

Following Cai and Mak [1990, see their Eq. (11)], the evolution of the eddy kinetic energy deduced from the baroclinic quasigeostrophic equations is

$$\frac{\partial K'}{\partial t} + \overline{\mathbf{u}}\nabla K' + \mathbf{u}'\nabla K' = \mathbf{E}'\overline{\mathbf{D}} + f\psi'\frac{\partial w'}{\partial z} + \nabla\cdot(\mathbf{u}'P'_a) + f\left[\frac{\partial}{\partial x}\left(\psi'\frac{\partial \chi'}{\partial x}\right) + \frac{\partial}{\partial y}\left(\psi'\frac{\partial \chi'}{\partial y}\right)\right], \tag{7}$$

where $K' = \frac{1}{2}\mathbf{u}'\mathbf{u}'$ is the eddy kinetic energy, the scalar product of $\mathbf{E}' = [\frac{1}{2}(v'^2 - u'^2), -u'v']$ and $\overline{\mathbf{D}} = (\partial\overline{u}/\partial x - \partial\overline{v}/\partial y, \partial\overline{v}/\partial x + \partial\overline{u}/\partial y)$ quantifies the barotropic transfer of energy from the basic state to the perturbation, and P'_a and χ' are two scalar fields representing the nondivergent and the irrotational part of the perturbation ageostrophic wind, respectively.

The integration of Eq. (7) on a horizontal layer gives

$$\frac{d}{dt}\int\int_z K'\,dx\,dy = \int\int_z \mathbf{E}\overline{\mathbf{D}}\,dx\,dy + \int\int_z f\psi'\frac{\partial\omega'}{\partial z}\,dx\,dy. \tag{8}$$

The last term of Eq. (8) is classically decomposed into two parts, which, in the framework of the two-layer model, can be written

$$\begin{aligned}\int\int_{z_u} f\psi'\frac{\partial w'}{\partial z}\,dx\,dy &= \int\int_{z_u}\frac{f}{2H}[\omega'_m(\psi'_l - \psi'_u) - \omega'_m(\psi'_u + \psi'_l)]\,dx\,dy \\ &= \frac{1}{2}C_I - C_F,\end{aligned} \tag{9}$$

$$\begin{aligned}\int\int_{z_l} f\psi'\frac{\partial w'}{\partial z}\,dx\,dy &= \int\int_{z_l}\frac{f}{2H}[\omega'_m(\psi'_l - \psi'_u) + \omega'_m(\psi'_l + \psi'_u)]\,dx\,dy \\ &= \frac{1}{2}C_I + C_F,\end{aligned} \tag{10}$$

where C_I and C_F are the surface integrals of the internal conversion (i.e., the baroclinic energy transfer from eddy potential energy to eddy kinetic energy and the ageostrophic geopotential flux, respectively). The eddy kinetic energy evolution in each layer is thus the addition of three terms: $C_K = \int\int_z \mathbf{E}'\overline{\mathbf{D}}\,dx\,dy$, which is purely barotropic, and C_I and C_F, which depend on the perturbations in the two layers; C_F is the vertical redistribution of energy between the two layers and it is straightforward that the sum of the right-hand sides of Eqs. (9) and (10) is equal to C_I.

3) BAROCLINICITY AND CONFIGURATION

The baroclinic conversion rate, denoted C_B, included in the perturbation total energy [$T' = \frac{1}{2}\lambda^{-2}(\psi'_u - \psi'_l)^2 + K'$] equation can be written in the two-layer model as

$$C_B = -\frac{1}{2\lambda^2}(\psi'_u - \psi'_l)[(\overline{v_u} - \overline{v_l})(u'_l + u'_u) - (\overline{u_u} - \overline{u_l})(v'_l + v'_u)] = \|\overline{\mathbf{B}}\|\,T'\cdot\text{conf}. \tag{11}$$

The ratio of C_B to T' can be written as the product of the modulus of the baroclinicity vector $\overline{\mathbf{B}} = 1/\lambda(\overline{\mathbf{u_u}} - \overline{\mathbf{u_l}})$ and a configuration term conf, the absolute value of which is always less than or equal to 1. Also, $\|\overline{\mathbf{B}}\|$ is the Eady parameter divided by 0.31; it quantifies the maximum amount of energy a perturbation can extract from its environment and is called the vertical shear strain rate or the baroclinicity.

Note that conf can be written as follows: conf = $||\mathbf{F}||/T'\cos(\mathbf{F}, \overline{\mathbf{B}})$, where $\mathbf{F} = \frac{1}{2}\lambda^{-1}(\psi'_u - \psi'_l)\,(-v'_l - v'_u, u'_l + u'_u)$. It is thus the product of two terms: the first one, $||\mathbf{F}||/T'$, quantifies the vertical phase tilt of the perturbation and is equal to 1 when this phase is equal to 90°; the other is the angle between the vertical axis connecting the upper and lower anomalies and the baroclinicity vector $\overline{\mathbf{B}}$. Thus, conf quantifies the efficiency of this baroclinic energy extraction; when conf = 1, the perturbations are optimally configured to extract energy (see Rivière and Joly 2006b for more details).

3. The shape and energetics of a vortex evolving in uniform horizontal and vertical shears

a. Initial conditions

In sections 3 and 4, the basic states are composed of uniform vertical and horizontal shears and are defined as follows:

$$\overline{\mathbf{u_u}} = (-\alpha y c_u^x + \alpha\lambda c^z)\,\mathbf{i}, \tag{12}$$

$$\overline{\mathbf{u_l}} = (-\alpha y c_l^x)\,\mathbf{i}. \tag{13}$$

The above scaling was chosen to quantify the relative values of the horizontal deformation rate $||\overline{\mathbf{D}}||$ and the vertical shear strain rate $||\overline{\mathbf{B}}||$ easily. It is straightforward that for $k \in \{u, l\}$, $\partial\overline{u_k}/\partial y = -\alpha c_k^x$ and if $c_u^x = c_l^x$, $H/\lambda\,\partial\overline{u}/\partial z = \alpha c^z$. It results that if $c_u^x = c_l^x = c^z$, $||\overline{\mathbf{D}}|| = ||\overline{\mathbf{B}}||$. These basic states will enable the behavior of cyclones to be mimicked on both the anticyclonic and cyclonic sides of zonal jets, even though a meridionally confined jet generally has a more complex profile than the linear ones employed here (see section 5). It should additionally be noted that only the baroclinic shear would lead to a growth rate of 0.64 day^{-1} for the most unstable normal mode in the Eady model.

The perturbations are defined with the help of the relative vorticity:

$$\text{for} \quad k \in \{u, l\},\ \zeta'_k = A'_k \exp\left[-\frac{(x' - x'_0 - \delta_{k=u} \cdot d')^2 + (y' - y'_0)^2}{r'^2}\right], \tag{14}$$

where A'_k is the vorticity maximum, $(x'_0 + \delta_{k=u} \cdot d', y'_0)$ is the coordinate of the perturbation center, and r' is its characteristic radius (common to both upper and lower anomalies). The upper anomaly is thus shifted to the west with respect to the lower one by the distance d'.

b. Pure barotropic case ($c_u^x = c_l^x$, $c^z = 0$, $\zeta'_u = \zeta'_l$, $d' = 0$)

To illustrate the behavior of a monopolar cyclonic vortex in uniform horizontal shear, a first nonlinear simulation was performed with the following parameters: $\lambda^{-2} = 0$ and for $k \in \{u, l\}$, $|c_k^x| = 1$, $A'_k = 8.10^{-5}\ \mathrm{s}^{-1}$ and $r'_k = 7.10^5$ m. The experiment with the cyclonic (anticyclonic) shear $c_u^x = c_l^x = 1(-1)$ is denoted C(A). The simulation is a nondivergent barotropic one, so only one of the two layers will be shown.

If the shear is anticyclonic (experiment A), the anomaly is strongly stretched by the basic state (Fig. 1). The orientation of the main axis of the perturbation varies slowly with time and its aspect ratio never ceases to increase: its value is over 15 after 36 h. In contrast, in C, the anomaly rotates quickly and its aspect ratio never exceeds 3.

In A, the total local tendency of vorticity (Fig. 2) is the result of the moderation of the background advection by the self-advection and is such that the vorticity mostly decreases up and downstream of the vortex and increases near its ends. The nonlinear advection has an effect opposite to that of the linear term: the former tends to make the perturbation axis rotate cyclonically. Therefore, two rotational effects mostly compensate each other so that the perturbation is stretched horizontally and spins only very slightly.

It can be seen in C (Fig. 2) that the advection by the basic state is rather small compared to the self-advection of the vortex and is decorrelated from it. It results that the total tendency is near zero at the ends of the structure (it does not extend horizontally) and the shape of the quadrupole is such that the main axis orientation changes strongly with time. Finally, the two rotational effects mostly act in the same sense.

To sum up, the combined effects of the linear and nonlinear terms in A make the perturbation tilt strongly along an axis that varies slowly throughout the simulation, whereas in C they act in such a way that the perturbation main axis changes quickly with time. Thus, the perturbation becomes more isotropic in C than in A. It should be noted that very similar results were obtained in a large range of $|c_k^x|$ and are qualitatively coherent with the analytical results of Kida (1981) concerning constant vorticity structures in uniform shears. The rate of change of the orientation of the elliptic vortex depends on the sum of the background vorticity and the perturbation vorticity. These two terms being of opposite signs in A, they tend to compensate each other, whereas in C their effects are additive.

c. Mixed barotropic–baroclinic case ($|c_u^x| = 1$, $|c_l^x| = 0.5$, $c^z = 1$)

To assess the role of the different baroclinic and barotropic tendency terms, a more realistic simulation of circular vortices in both horizontal and vertical shears was carried out. The parameters of the simulation were the following: $\lambda = 4.5\ 10^5$ m, $A'_u = A'_l = 8 \times 10^{-5}\ \mathrm{s}^{-1}$, $d' = 10^6$ m $\approx 2.2\lambda$, and $r' = 7 \times 10^5$ m $\approx 1.5\lambda$. As before, the experiment with the cyclonic (anticyclonic) shear is denoted with the letter C (A).

In the presence of both horizontal and vertical shears (Fig. 3), the shape evolution of initially circular vortices is qualitatively similar to that obtained in the purely barotropic case: the cores of the upper and lower structures, after a first stage of moderate stretching, become durably circular in C whereas they are strongly horizontally stretched in A, with an almost constant orientation. Moreover, the patterns of the linear and nonlinear tendencies in the vorticity equation (Fig. 4) are close to the pure barotropic case (Fig. 2). In A, the tendency is negative both upstream and downstream of the vortex and positive near its northern end, which leads to a horizontal stretching of the structure. The tendencies in C are very close to those obtained in the barotropic experiment; the main differences arise because the tendencies are not symmetric quadrupoles since both linear and nonlinear stretching terms are roughly dipolar (not shown). In addition, these observations, which are clearly illustrated with the values chosen above, were also found for a large range of parameters.

There is also a marked difference in the relative position of the upper and lower anomalies. In A, the horizontal distance between the two structures is almost constant with time, the lower one lying downstream of the upper. In C, the two anomalies turn quickly around one another: after 36 h, the center of the lower anomaly is even upstream of the upper one.

During the first 30 h of the simulation, the amplitude of the perturbation streamfunction and that of the vorticity grow more rapidly in C than in A (Figs. 5a,b). Nevertheless, during the following day, even though the

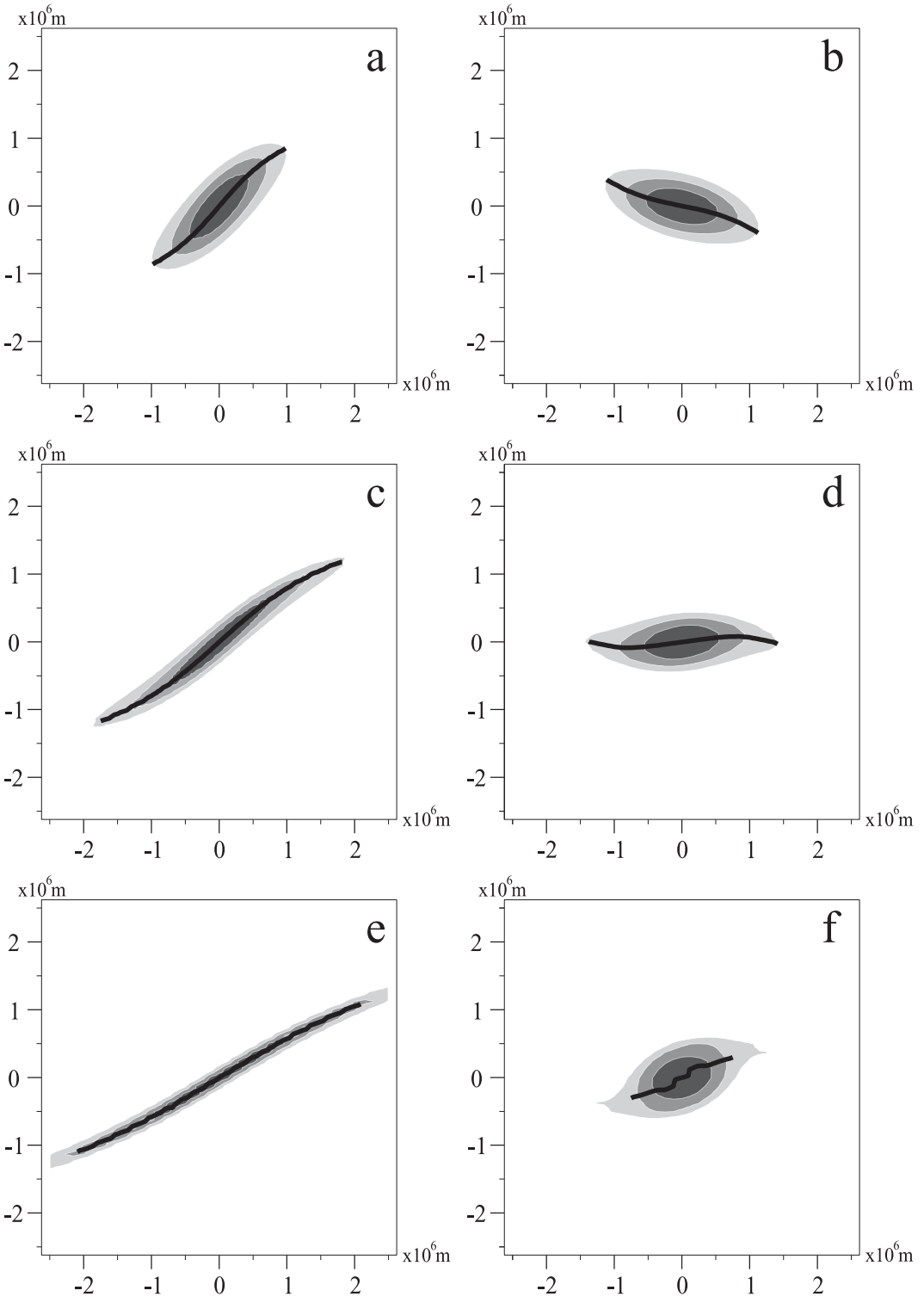

FIG. 1. Evolution of the perturbation relative vorticity for an initially circular cyclonic vortex embedded in (left) an anticyclonic and (right) a cyclonic shear after (a),(b) 12, (c),(d) 24, and (e),(f) 36 h barotropic simulations ($|c_k^x| = 1$). To highlight the axis of the vorticity anomaly, the black line is a section of the 0-isoline of the field that contains the scalar product of the vorticity gradient and the first eigenvector of the Jacobian matrix of vorticity.

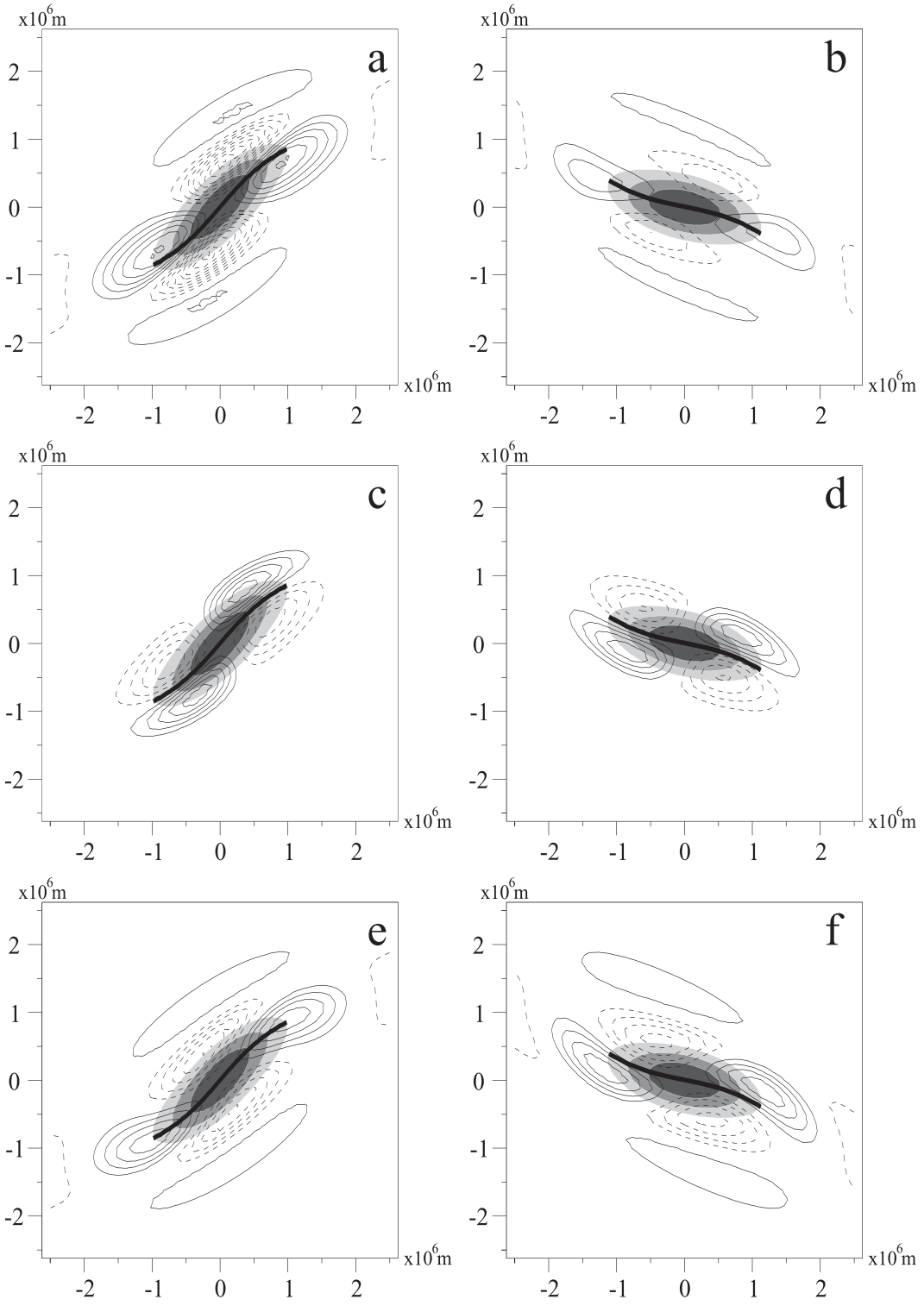

FIG. 2. Vorticity tendency terms for the same barotropic simulation and the same time as (left) Fig. 1a and (right) Fig. 1b. (a),(b) Advection by the basic state, (c),(d) nonlinear advection, and (e),(f) total tendency, with solid and dashed lines representing positive and negative values, respectively (contour interval of 2×10^{-10} s^{-2}). Gray shadings indicate the perturbation vorticity (interval of 2×10^{-5} s^{-1}). The advection of the background vorticity by the perturbation, which is included in the total tendency, is always considerably smaller than the other tendency terms and is therefore not shown individually.

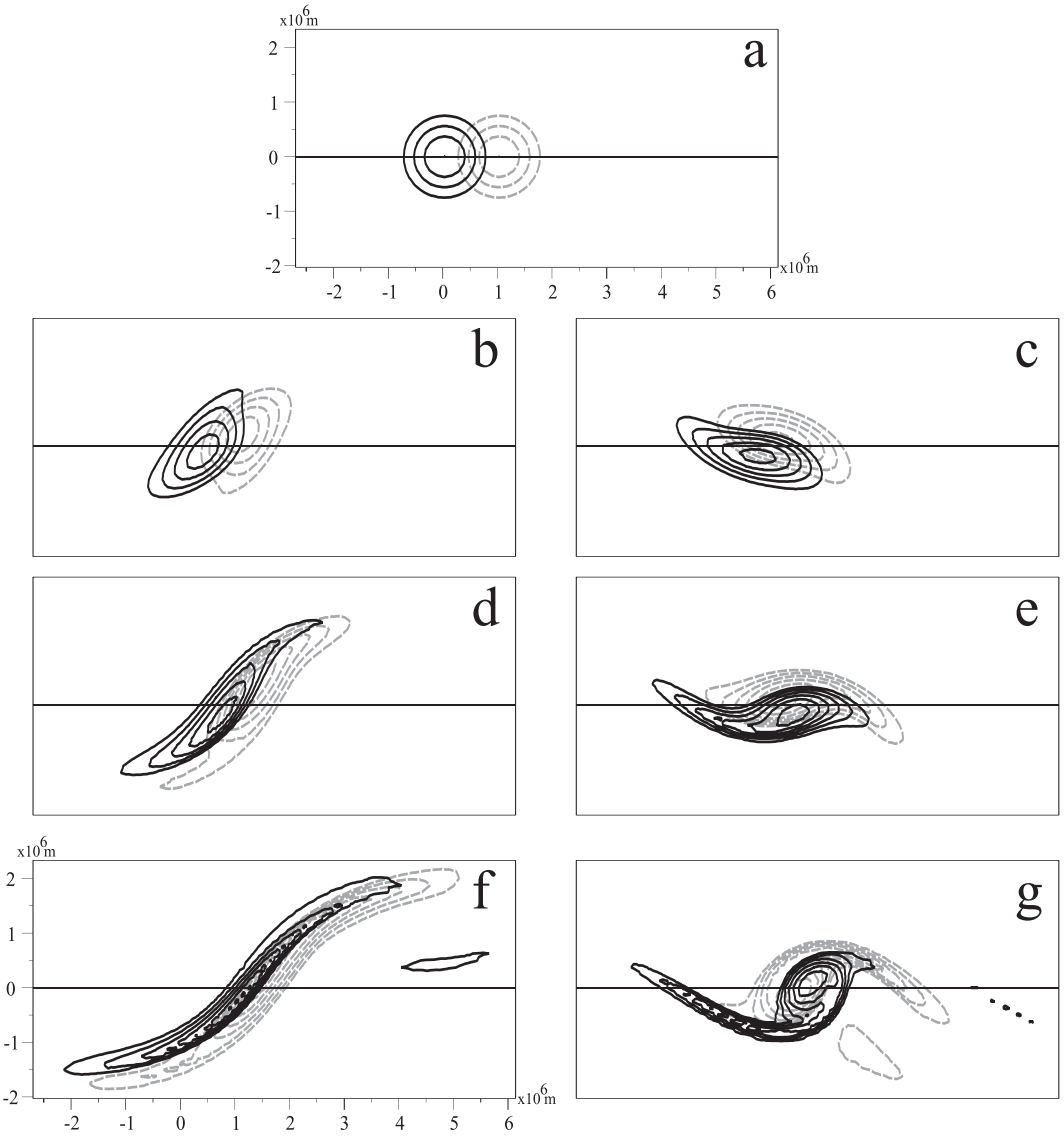

FIG. 3. Evolution of the upper-layer (solid) and lower-layer (dashed) vorticity anomalies (interval of $2 \times 10^{-5}\ s^{-1}$) at $t = 0$, 12, 24, and 36 h from top to bottom in the two-layer baroclinic simulation ($|c_x^u| = 1$, $|c_x^l| = 0.5$, $c_z = 1$): (left) anticyclonic shear; (right) cyclonic shear.

values of $|\zeta'|_{\max}$ in A and C are very similar, $|\psi'|_{\max}$ does not grow and even decreases in A, whereas it still deepens in the cyclonic case. Because vorticity is equal to the Laplacian of the streamfunction, this discrepancy is mostly due to the larger horizontal stretching in A.

The energy budget in the lower layer (Figs. 5c,d) shows that the vertical geopotential flux plays a secondary role in the kinetic energy variation, which is thus primarily controlled by the internal C_I and barotropic C_K conversions. As expected, the barotropic conversion, which is initially zero because of the structure isotropy, is largely negative during the whole simulation in A. This can be explained by the strong elongation of the perturbation along the direction of the background shear. In contrast, because of the moderate change of shape of the perturbation core in C, C_K is less negative than in A and is even near zero during most of the second day of the simulation. In conclusion, the barotropic conversion tends to notably lessen the perturbation energy in A whereas it has a small negative contribution in C.

Another marked difference between C and A is visible: after 12 h, C_I falls strongly in C whereas it remains at high levels in A. Even if $|c_u^x| = c^z$, the variation of C_I prevails over that of C_K so that the perturbation kinetic energy growth is higher in A than in C. The variable C_I quantifies the energy exchange between the perturbation potential

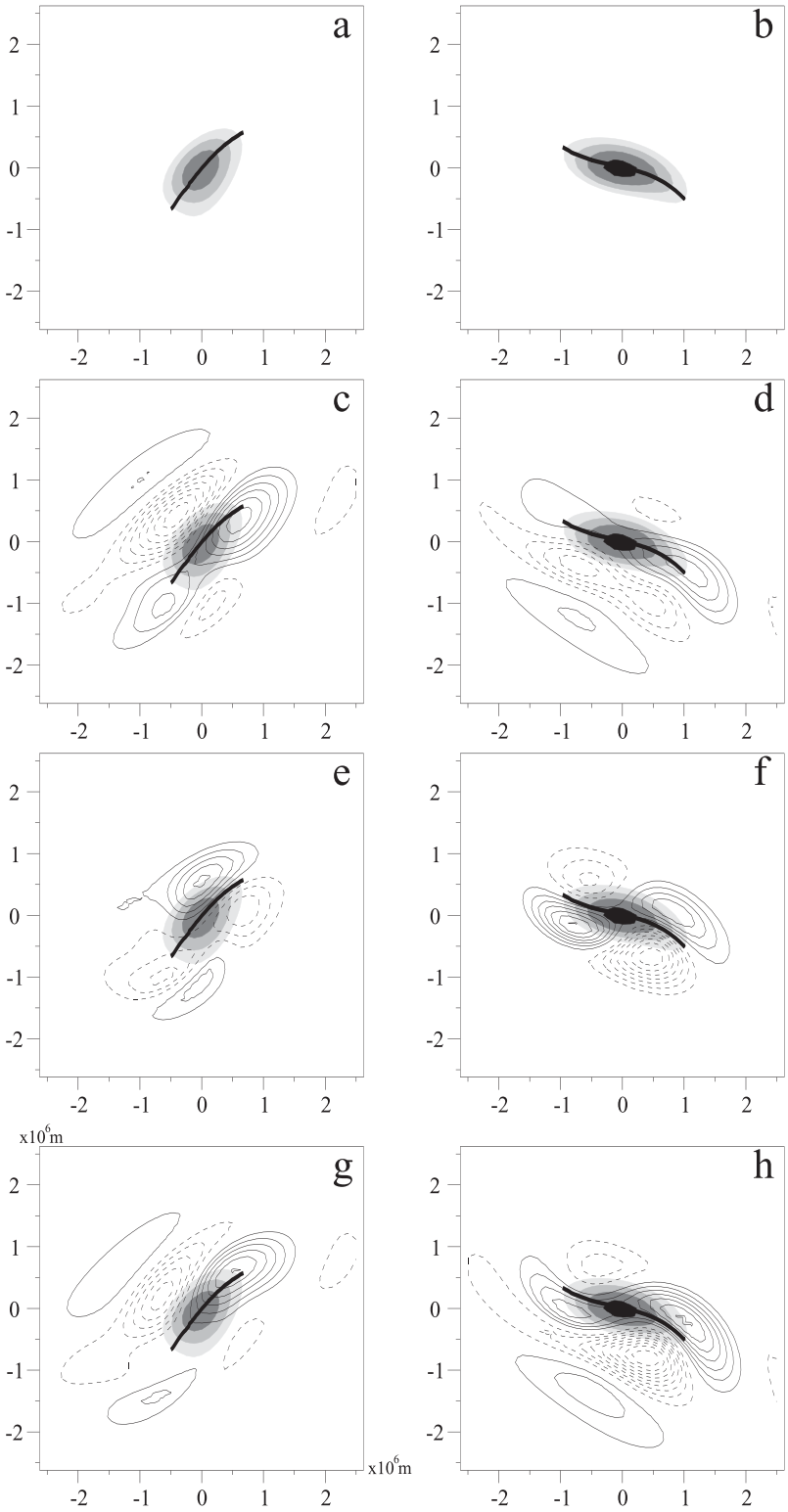

FIG. 4. Vorticity tendency terms for the same two-layer baroclinic simulation and the same time (12 h) as (left) Fig. 3b and (right) Fig. 3c. (a),(b) Lower-layer vorticity, (c),(d) linear terms, (e),(f) nonlinear terms, and (g),(h) total tendency terms, with solid and dashed lines representing positive and negative values, respectively (interval of $10^{-10}\,s^{-2}$). The thick black line stands for the anomaly main axis. The panels are centered at the position of the lower-layer perturbation vorticity maximum.

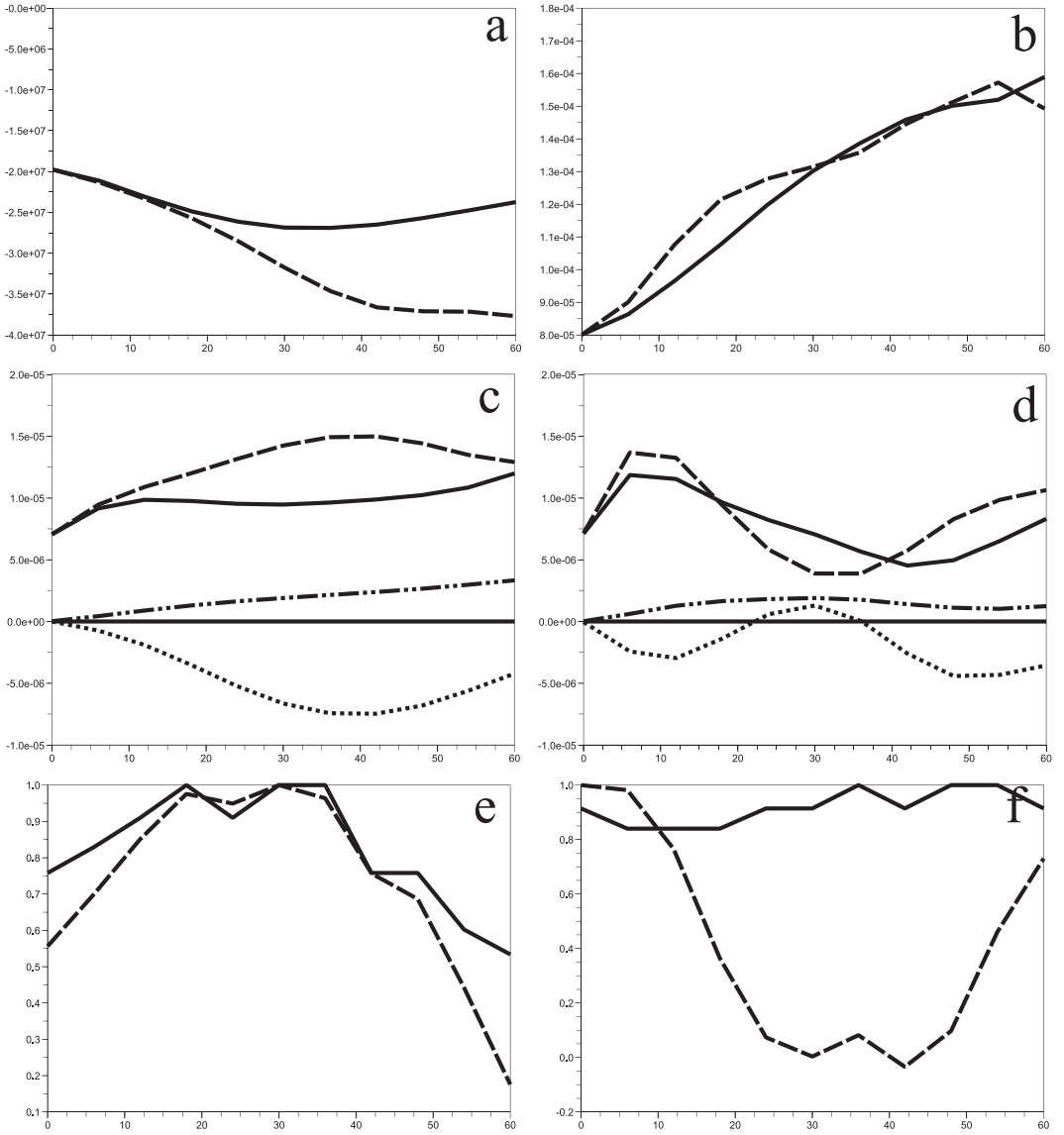

FIG. 5. Same simulation as in Fig. 3, showing the time evolution of (a) the lower-layer streamfunction minimum and (b) the perturbation vorticity maximum (solid line for the anticyclonic case, dashed line for the cyclonic case). (c),(d) Kinetic energy budget at the lower layer for the (c) anticyclonic and (d) cyclonic cases (dashed: internal conversion; dotted: barotropic conversion; dashed–dotted: vertical geopotential fluxes; solid: rate of kinetic energy evolution, which equals the sum of all the conversions). (e),(f) Baroclinicity $||\mathbf{B}||$ (solid) and conf $||\mathbf{B}||$ (dashed) scaled by their respective maximum values.

and kinetic energy and is the integrated correlation of the perturbation vertical velocity and the perturbation potential temperature. Figure 6 shows these two fields at the middle of the domain at $t = 30$ h. In A, the upper anomaly induces positive vertical velocity downstream of it, where the lower cyclonic (and thus warm) anomaly is situated. In other words, the two anomalies are sustainably favorably tilted for a strong baroclinic interaction. In contrast, in C the areas of significant vertical velocity are far from the potential temperature anomaly and are less intense than in A. The result is that the product of vertical velocity and potential temperature is small everywhere. In that case, the fact that the upper perturbation is east of the lower one induces a poor configuration for baroclinic growth. This can also be diagnosed from the configuration term: the product $\| \overline{\mathbf{B}} \|$ conf is quite close to $\| \overline{\mathbf{B}} \|$ in A (Fig. 5e) whereas it is much weaker than $\| \overline{\mathbf{B}} \|$ in C (Fig. 5f). To sum up, the relative position of the upper and lower anomalies is responsible for the strong energy difference between the two simulations. This position is the result of both the

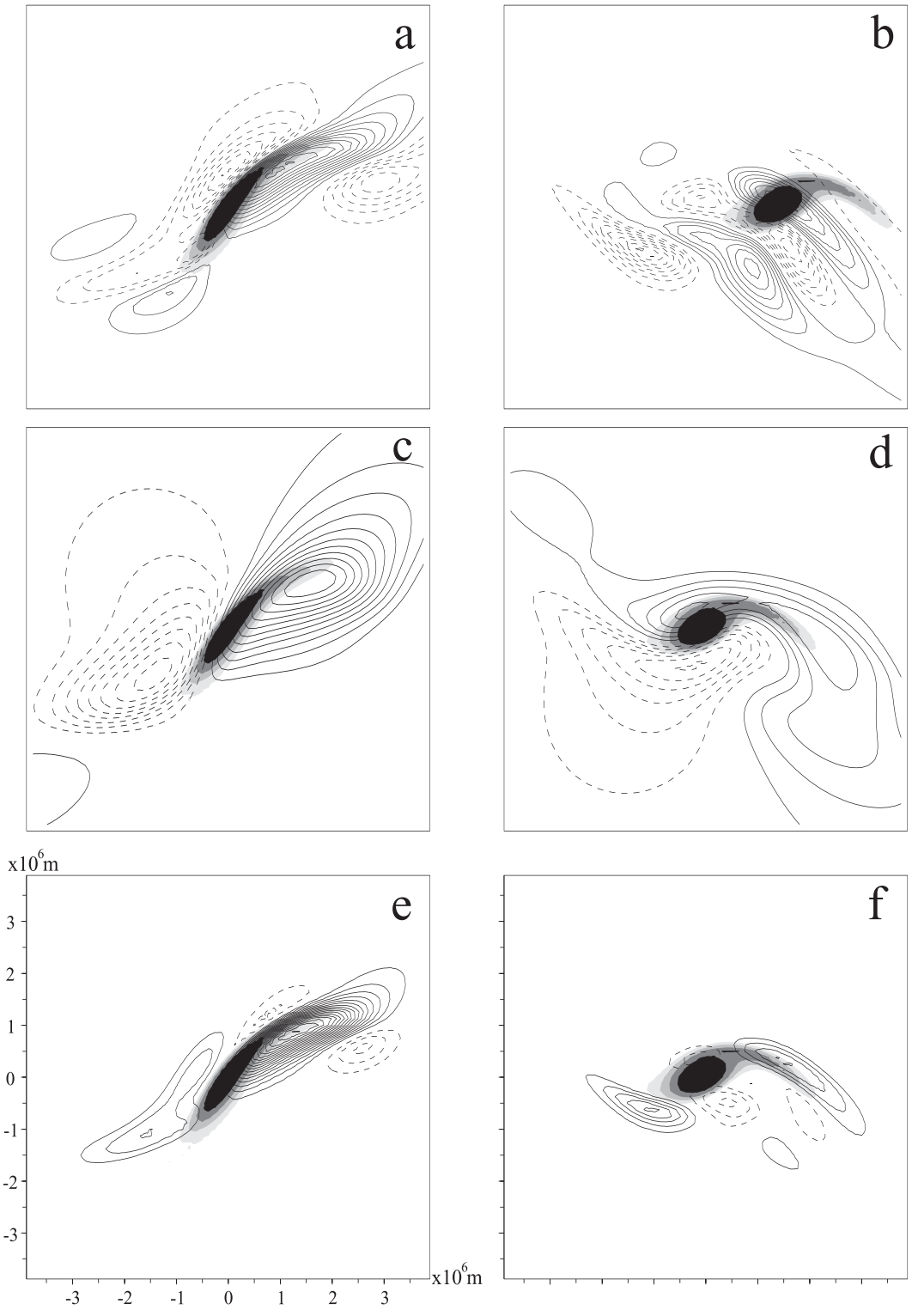

FIG. 6. (from top to bottom) Vertical stretching $(fw)/(2H)$ (interval of 6×10^{-11} s^{-2}), potential temperature (interval of 1 K), and their local product (interval of 5×10^{-10} K s^{-2}); the solid and dashed lines represent positive and negative values, respectively. (all panels) Perturbation vorticity (gray shadings; contour interval of 2×10^{-5} s^{-1}). Same simulation as Fig. 3 at $t = 30$ h. (left) Anticyclonic and (right) cyclonic shear. The maximum of vorticity is located at the center of the panels.

self-rotation of the anomalies around one another (which exists already without horizontal shear) and the rotation effect of the basic state. The latter counteracts the self-rotation if the background shear is anticyclonic and contributes to it if it is cyclonic.

Other experiments with the same vertical shear but with modifications of the value of the horizontal shears have been conducted; they do not qualitatively change the results. For instance, in a simulation with the same horizontal shear in both layers ($c_u^x = c_l^x = 1$), the barotropic conversion has a stronger amplitude than in the case shown in Fig. 5, but the qualitative differences between the cyclonic and anticyclonic shear cases are still the same. To conclude, the sign of the basic-state shear is of prime importance as far as the perturbation deepening and shape are concerned. As long as a finite-amplitude vortex lies in an anticyclonic shear, although it tends to be strongly stretched and loses energy barotropically, it does not become weaker as a whole because its favorable configuration leads to efficient baroclinic processes. In contrast, in cyclonic shear (notably on the north side of a westerly wind) the vortex does not lose so much energy via barotropic interaction because of its more isotropic structure, but at the same time its vertical structure is less efficient in extracting energy baroclinically. In the latter case, because of the rotation of the lower anomaly relative to the upper one, the initially well-configured baroclinic configuration is rapidly lost whereas in the former case, it is well maintained over time. Because of these structural differences, the growth is more transient and more pronounced in the beginning of the cyclonic simulation whereas it is more sustained in the anticyclonic case.

4. Nonlinear dynamics pushing cyclones northward

The last section shed some light on the shape and energetics of structures embedded in horizontal shears that typically mimic both sides of a zonal jet. This section is dedicated to the examination of the mechanisms controlling the trajectory of a surface cyclone and especially its meridional shift.

a. Preliminaries

In all the experiments of the preceding section, no clear meridional shift of the anomalies can be noted (Fig. 3), except for a slight displacement in the cyclonic shear due to the rotation of one anomaly around the other. In the field of tropical cyclones (Shapiro 1992) and oceanic vortices (McWilliams and Flierl 1979), it has long been recognized that a background PV meridional gradient may be at the origin of the meridional shift of vortices. To assess the impact of such a latitudinal variation on the trajectories of midlatitude synoptic-scale vortices, simulations were run with $\beta = \beta_0$ and $\beta = 3\beta_0$, $c_u^x = 2$, $c_l^x = \delta$, and $c^z = 1$. Here δ was set to 0 for a pure baroclinic simulation and to ± 1 for simulations with horizontal shear. Even though the result in the tropical cyclone motion is well known in a barotropic context, it is less obvious for midlatitude depressions where baroclinic interaction plays a central role.

Following Eqs. (1), (2), (12), and (13), the meridional variation of the background PV can be written as follows:

$$\frac{\partial \overline{q_u}}{\partial y} = \beta + \alpha\lambda^{-1}c^z - \alpha\lambda^{-2}(c_u^x - c_l^x)y \quad \text{and} \tag{15}$$

$$\frac{\partial \overline{q_l}}{\partial y} = \beta - \alpha\lambda^{-1}c^z + \alpha\lambda^{-2}(c_u^x - c_l^x)y. \tag{16}$$

If $\beta = 0$, $\partial\overline{q_u}/\partial y$ and $\partial\overline{q_l}/\partial y$ have the same amplitude but opposite signs. As noted in the previous section, no meridional displacement is detected in this case. In accordance with classic observations, c_u^x is always of greater absolute value than c_l^x. By increasing β, $\partial\overline{q_u}/\partial y$ thus increases and reaches stronger positive values and $\partial\overline{q_l}/\partial y$ becomes closer to zero (it is positive when $\beta > 3.4\beta_0$). For the values considered (β_0 and $3\beta_0$), $\partial\overline{q_u}/\partial y$ and $\partial\overline{q_l}/\partial y$ are of opposite signs. Note finally that the vertical average of the PV meridional gradient is here reduced to β.

b. Results

As mentioned previously, in the two-layer experiment the path of the surface vorticity anomaly in an f plane stays at almost the same latitude (see the dashed black lines in Figs. 7a,b). When β is included (see the solid black and gray lines in Figs. 7a,b), there is a systematic northwestward shift. The westward displacement is coherent with the well-known linear β effect whereas the northward shift is similar to the result of the nonlinear barotropic β drift. The addition of an initial upper anomaly makes this northwestward motion faster.

To highlight the role of the interaction between the upper and the lower layers, we integrate Eq. (3) in the lower layer by keeping the perturbation streamfunction in the upper layer equal to zero ($\psi_u' = 0$). This is tantamount to integrating a barotropic equivalent model, as follows:

$$\frac{\partial}{\partial t}q_l' + \mathbf{u_l'}\nabla q_l' + \mathbf{u_l'}\nabla\overline{q_l} + \overline{\mathbf{u_l}}\nabla q_l' = 0, \quad \text{where}$$

$$q_l' = \Delta\psi_l' - \lambda^{-2}\psi_l'. \tag{17}$$

The results of the barotropic equivalent simulation (Fig. 7c), in which the role of the upper layer is neutralized, are at stark variance with those obtained in the full two-layer model. All trajectories are southeastward and

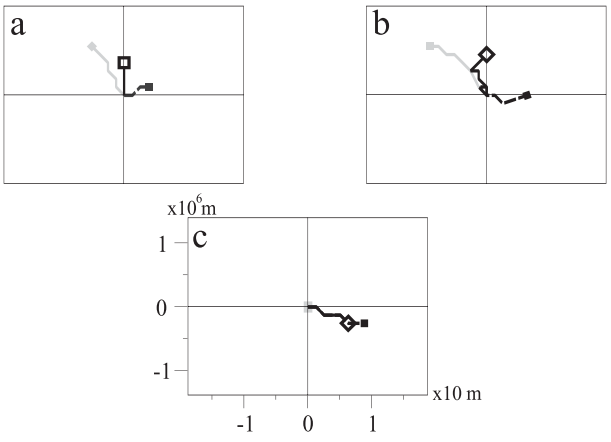

FIG. 7. Trajectories of the lower vorticity anomaly from 0 to 48 h in (a) a two-layer baroclinic simulation without an initial upper anomaly, (b) a two-layer baroclinic simulation with an initial upper anomaly, and (c) a barotropic-equivalent simulation. All simulations are run without basic-state horizontal shears. Simulations with $\beta = 0$, $\beta = \beta_0$, and $\beta = 3\beta_0$ are represented by dashed black, solid black, and solid gray lines, respectively.

become shorter as β increases. This is consistent with the fact that in this experiment the structure only feels the lower part of its environment, the PV gradient of which is oriented southward ($\partial\overline{q_l}/\partial y < 0$) when $\beta = 0$ and becomes less and less intense with increasing β. The sum of the vorticity tendencies, which is the combination of the linear terms and the nonlinear advection, is a southeast–northwest dipole.

A comparison with the full two-layer baroclinic simulation for $\beta = 0$ and no initial upper anomaly (second column of Fig. 8) shows that the difference in the trajectory originates in the nonlinear vertical stretching term, which has a large positive northward component and is of greater amplitude than the southward nonlinear advective tendency. Overall, the vorticity tendency induces a small poleward displacement. The interaction between the lower and upper anomalies (the latter created through baroclinic interaction of the lower anomaly and the jet) is responsible for a transient northward displacement in the $\beta = 0$ purely baroclinic experiment, linked with the winding up of the upper and lower anomalies.

Increasing β and adding an initial upper anomaly makes the poleward tendency more pronounced. Note that when $\beta > 0$, both nonlinear terms participate in the poleward shift. The last two experiments ($\beta = 3\beta_0$, with or without an initial upper anomaly) confirm the strong poleward tendency observed in Fig. 7. The nonlinear advective term is positively oriented toward the north. It should be noted that this term has a nonnegligible zonal component, which can be explained by the effect of the parent cyclone on the dipole created through linear advection of PV gradient.

Adding a linear horizontal shear ($c_u^x = \pm 1$, $c_l^x = \pm 0.5$) does not qualitatively change the meridional shift: a clear poleward displacement in both the cyclonic (Figs. 9a,c) and the anticyclonic cases (Figs. 9b,d) was obtained for $\beta > 0$ with, incidentally, a faster movement in the latter case. Moreover, Table 2 shows that the differences in the zonal displacement in the mixed barotropic–baroclinic basic winds can be explained simply by advective mechanisms. For instance, in the cyclonic experiment with an initial upper anomaly, the zonal displacement speed is in excess of -16.4 m s^{-1} when compared to the no-shear experiment. This value is mostly the average between the upper- and lower-layer wind associated with the cyclonic component of the environmental wind. The addition of a barotropic component to the basic state wind only adds an advective zonal component, linked with a steering level near midtroposphere when an upper anomaly exists or near the lower layer when the anomaly is mostly restricted to that layer.

It should be noted that the relative vorticity was the most robust variable examined (more so than streamfunction or PV) when the parameters (size of perturbations, basic flow intensity, etc.) were modified. In some experiments, it was also observed that even when the perturbation relative vorticity maximum stayed at the same latitude, the streamfunction or the PV maximum could shift northward because of scale relations.

To sum up, no significant latitudinal motion of surface cyclones is detected if $\beta = 0$, whereas a clear systematic poleward shift appears for $\beta > 0$ (i.e., for a positive vertically integrated meridional PV gradient). This displacement is faster with the presence of an initial upper cyclonic anomaly and slightly more pronounced in an anticyclonic shear. The different experiments suggest that the interaction with the upper layer makes the surface cyclone feel the orientation of the PV gradient integrated over the whole troposphere, which is poleward, rather than the local lower-layer southward PV gradient.

5. Jet crossing in a meridionally confined zonal jet

This section examines a more realistic simulation in which a cyclonic vortex is initially situated south of a meridionally confined zonal jet.

a. Initial conditions

The basic state is defined as follows:

$$\overline{\mathbf{u_u}} = c_u^c \exp\left[-\left(\frac{y - y_0}{d}\right)^2\right]\mathbf{i} \quad \text{and} \tag{18}$$

$$\overline{\mathbf{u_l}} = c_l^c \exp\left[-\left(\frac{y - y_0}{d}\right)^2\right]\mathbf{i}, \tag{19}$$

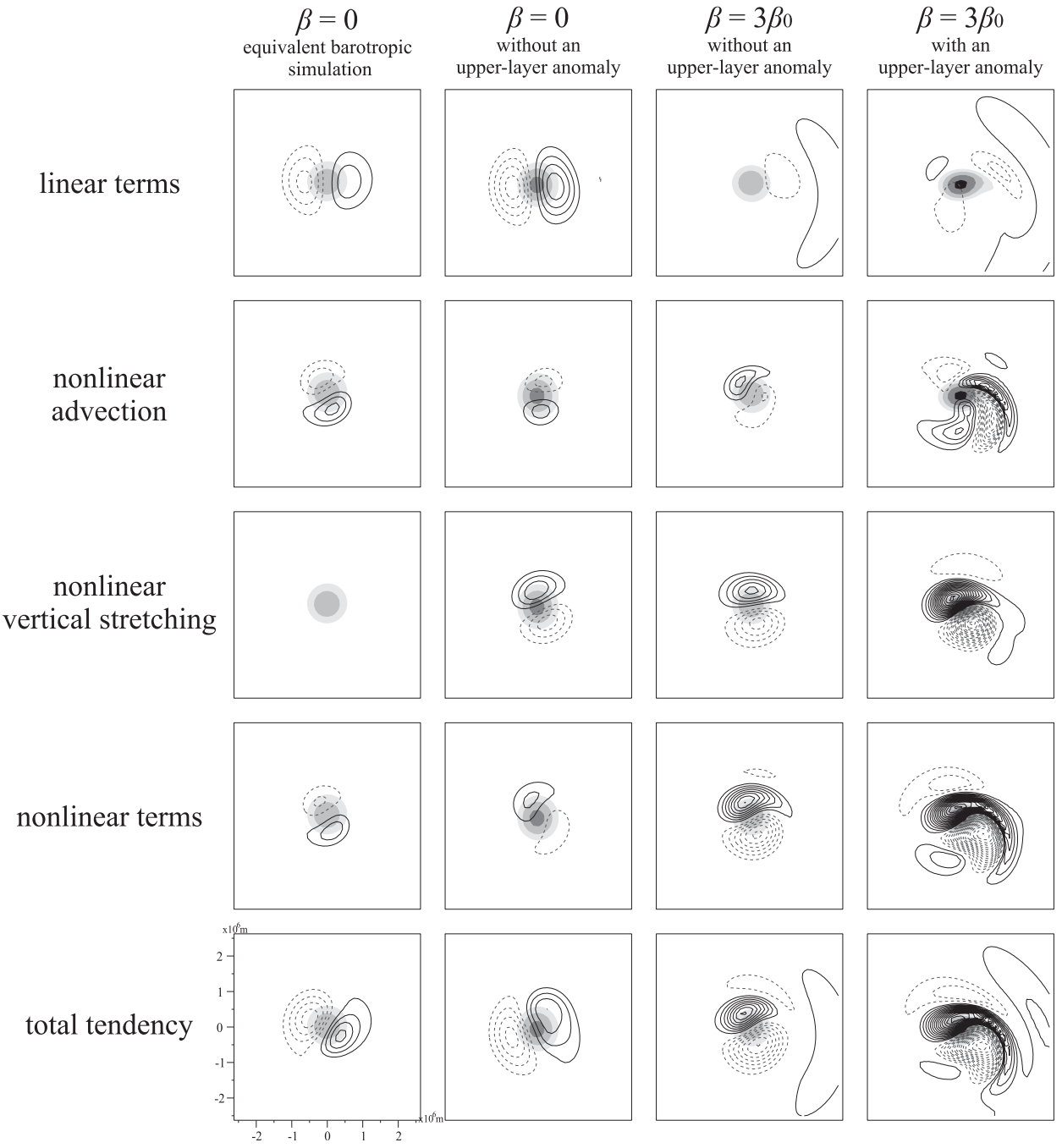

FIG. 8. Vorticity tendency terms at $t = 24$ h ($c_x^u = 0$, $c_x^l = c_z = 1$). (from top to bottom) Sum of all linear terms, nonlinear advection, nonlinear vertical stretching, sum of all nonlinear terms, and total tendency (contour interval of 10^{-10} s^{-2}). (all panels) Perturbation vorticity (contour interval of 2×10^{-5} s^{-1}). (far left column) Here $\beta = 0$; equivalent barotropic simulation. (from left to right) Two-layer baroclinic model: (second column) $\beta = 0$ without upper-layer anomaly, (third column) $\beta = 3\beta_0$ without an upper-layer anomaly, and (far right column) $\beta = 3\beta_0$ with an upper-layer anomaly.

where y_0 is the mean latitude of the domain, $d = 1400$ km $\approx 3.1\lambda$ is the jet characteristic width, and $c_u^c(c_l^c)$ is the maximum value of the jet wind speed in the upper (lower) layer. Two sets of values are used to define two basic states: $J_{50}(c_u^c = 50$ m s^{-1}, $c_l^c = 25$ m s$^{-1})$ and $J_{30}(c_u^c = 30$ m s^{-1}, $c_l^c = 5$ m s$^{-1})$. These two jets have different barotropic components, the maximum of which is equal to 1.25α in J_{50} (0.75α in J_{30}), but share the same baroclinicity field. Figure 10 reproduces the wind and the PV gradient for J_{50}. The latter is poleward in the upper

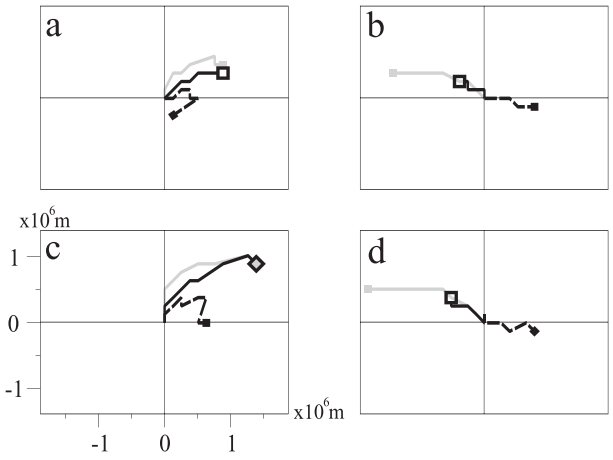

FIG. 9. Same simulation as in Figs. 7a,b but with (a),(c) anticyclonic and (b),(d) cyclonic shear added to the basic state.

TABLE 2. Zonal velocity values (m s^{-1}) of the difference between mixed barotropic–baroclinic experiments and pure baroclinic experiment. The speed value is calculated as the difference between the zonal speed obtained in the mixed barotropic–baroclinic experiment and the zonal speed observed in the pure baroclinic one after 48 h of simulation. The wind speeds are the values of the barotropic component of the wind specified at the latitude reached by the center of the lower-layer perturbation.

Upper anomaly?	Exp.	Speed	Upper-level wind	Lower-level wind
With	C	−16.4	−21	−10.5
	A	8.7	12	6
Without	C	−5.5	−12	−6
	A	5.5	9	4.5

layer and equatorward in the lower layer with weaker amplitude. This bias toward a poleward component results from the poleward relative vorticity gradient in both layers ($-\partial^2 u_u/\partial y^2 > 0$ and $-\partial^2 u_l/\partial y^2 > 0$). Note that the vertically averaged PV gradient $[-\frac{1}{2}(\partial^2 u_u/\partial y^2 + \partial^2 u_l/\partial y^2)]$ is much stronger in J_{50} than in J_{30}.

The anomalies have the same characteristics as those used in section 3 and are initially situated 1000 km south of the jet axis.

b. Nonlinear results

Figure 11 (the experiment with J_{50}) shows that the lower anomaly clearly shifts to the north, whereas the upper anomaly mostly moves toward the center of the jet. This can be interpreted as the effect of the poleward orientation of the vertically averaged background PV gradient according to the previous section.

The shape of the lower anomaly has also an evolution similar to what could be expected from section 4: as long as it is on the south (anticyclonic) side of the jet, the background shear stretches the anomaly horizontally along a southwest–northeast orientation. After the jet crossing (about $t = 36$ h), the main core of the cyclone becomes much more isotropic (Fig. 11f). The evolution in J_{30}, which has a smaller barotropic component, is quite different: the shape of the lower anomaly is less variable with time, it crosses the jet later (at around $t = 55$ h) and less clearly than in J_{50} (Fig. 12). The discrepancy in the aspect ratio and orientation can be explained by the fact that although the barotropic and baroclinic components of the jet have almost the same value as that prescribed in section 3c at the initial position of the anomalies, the ratio between barotropic and baroclinic shear is obviously weaker near the jet axis and the horizontal anticyclonic shear is therefore not strong enough to counteract the rotation of upper and lower anomalies around one another. Because the barotropic component of J_{30} is smaller than that of J_{50}, the anomaly is more isotropic than in the latter jet.

These different shape variations between the two simulations have a strong impact on the relative evolution of

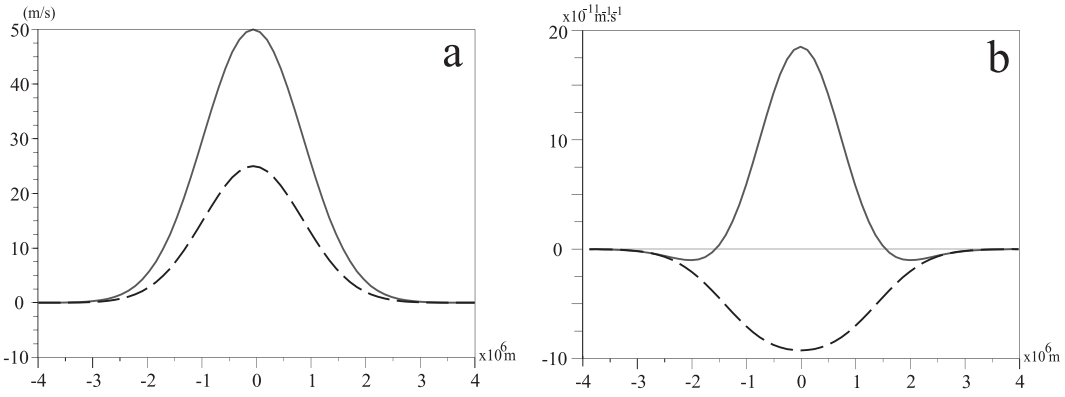

FIG. 10. Meridional profiles of the J_{50} (a) wind and (b) PV gradient meridional component. The solid and dashed lines correspond to the upper and lower layers, respectively.

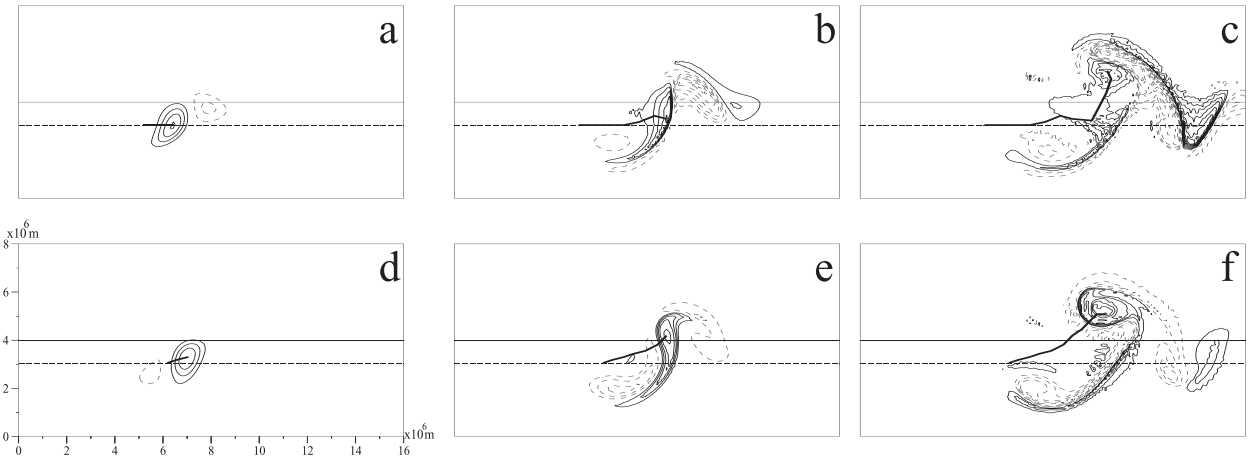

FIG. 11. Nonlinear evolution of the (top) upper- and (bottom) lower-layer cyclonic vortices, which are initially vertically tilted and situated on the southern side of J_{50}, at (a),(d) 12, (b),(e) 36, and (c),(f) 60 h. Perturbation relative vorticity is in solid (positive values) and dashed lines (negative values); interval of 2.5×10^{-5} s^{-1}. The solid thin black line stands for the jet axis and the dashed line for the initial latitude of the anomalies. The trajectories of the vorticity maxima are marked in thick solid black.

vorticity and streamfunction absolute maxima because of the scale relation between these two fields (Figs. 13a,b). The vorticity maximum increases (Fig. 13b) first faster in J_{30} than in J_{50} but is almost constant for two days after $t =$ 36 h whereas the rate of vorticity change abruptly increases for about one day at $t = 40$ h in J_{50}. In J_{30}, the rate of change of the streamfunction minimum (Fig. 13a) is approximately constant with time, whereas a marked change of slope can be observed in J_{50} during the jet crossing.

The differences of behavior between J_{50} and J_{30} are now interpreted with the help of an energy budget. Before starting the analysis, let us look at the effect of a nonzero vertically averaged PV gradient. Figure 14 illustrates the energy budget of the same simulation as Fig. 5 but with $\beta = 3\beta_0$. The inclusion of the β term does not qualitatively change the differences between cyclonic and anticyclonic shears. In the former, the kinetic energy growth rate is strong only in the beginning of the simulation (for about 12 h) and quickly decreases thereafter, whereas in the anticyclonic case the growth lasts longer. However, a marked difference is visible in the vertical geopotential fluxes: they are strongly negative in both cases while they play a negligible role in the energy budget for $\beta = 0$.

Figures 13c–f illustrate the energy budget of a portion of the lower layer, which is defined as the restriction of the anomaly to a square around the maximum of the lower-layer vorticity. This restriction necessitates the existence of an additional term in the energy budget, namely the horizontal energy redistribution fluxes. Tests were performed on the size of this square and revealed that the deductions made below are qualitatively robust

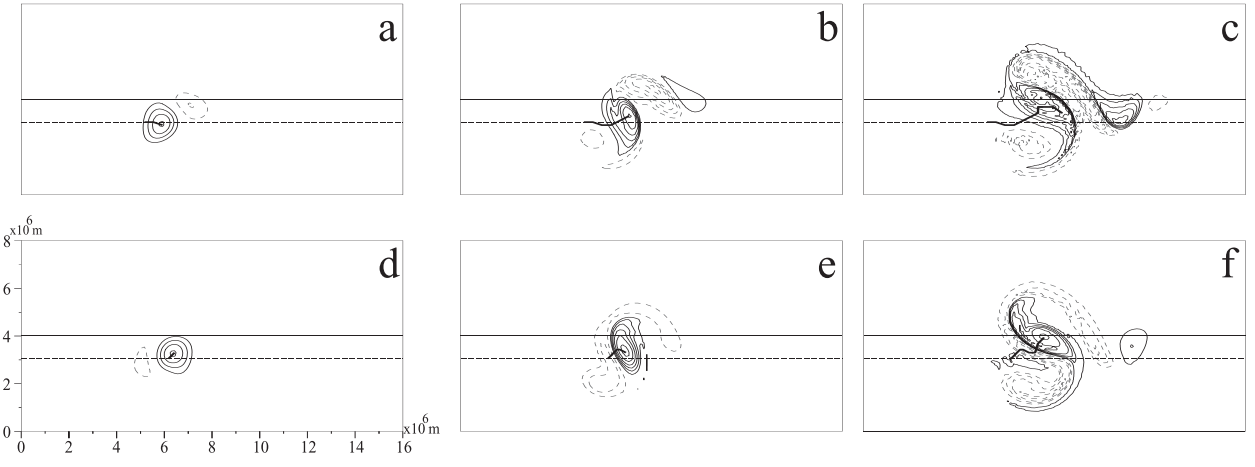

FIG. 12. As in Fig. 11, but with the J_{30} jet.

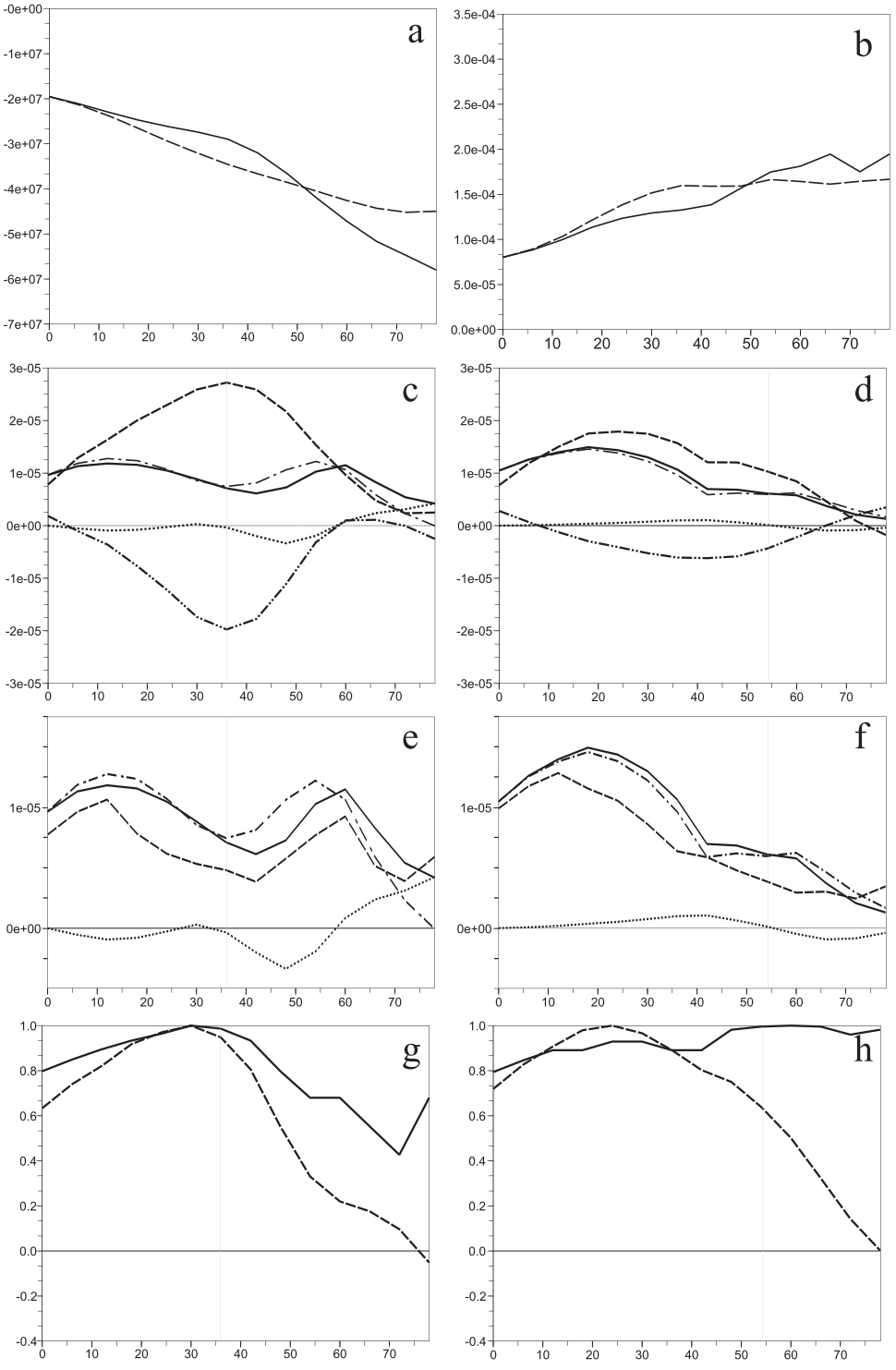

FIG. 13. Time variation up to 78 h of (a) the streamfunction minimum, (b) the vorticity maximum. In (a) and (b), evolution in (solid) J_{50} and (dashed) J_{30}. (c),(d) Variation of the kinetic energy conversion rates at the lower layer (long-dashed line, C_I; dotted line, C_K; dashed–double-dotted line, C_F; dashed–single-dotted line, sum of C_I and C_F; solid line, sum of C_I, C_K, and C_F), (e),(f) (dashed–dotted line, sum of C_I and C_F; dotted line, C_K; solid line, sum of C_I, C_K, and C_F; dashed line, kinetic-energy rate of change), (g),(h) baroclinicity and baroclinic conversion divided by total energy. (c)–(h) (left) Jet J_{50}; (right) J_{30}. Two-layer baroclinic simulation. The vertical lines denote the time when the jet crossing occurs.

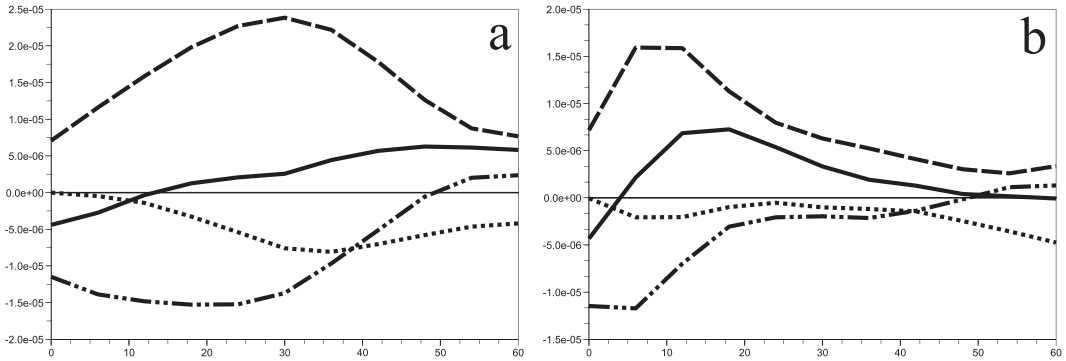

FIG. 14. (a),(b) As in Figs. 5c,d, respectively, but for $\beta = 3\beta_0$.

when the size varies, provided that no other structure is included in the domain. It should first be noted that in both simulations the barotropic conversion C_K is small in comparison to the other terms. The horizontal flux is almost constant and negative throughout, which can be related to downstream and upstream development (Orlanski and Sheldon 1995). The variation of the kinetic energy growth rate is thus mainly controlled by the vertical geopotential flux C_F and the internal conversion C_I. In J_{50}, these two contributions mainly evolve in the same way but in opposite directions. Note in particular that according to Fig. 14, C_F is strongly negative during the jet crossing when the anomaly is embedded in a large PV gradient. The kinetic energy growth rate decreases during the 18 h before the jet crossing and then increases for about 18 h after it, starting from 5×10^{-6} s^{-1} (after 42 h) and reaching 10^{-5} s^{-1} (after 60 h). This is equivalent to the growth rate almost doubling at the jet crossing. In J_{30}, the balance between C_I and C_K is different: C_I is maximum one day before the crossing of the jet and then decreases strongly whereas C_F reaches its minimum a few hours before this crossing. The sum of these two terms has a maximum growth rate during the first 36 h and decreases strongly before the anomaly crosses the jet axis because of both a decrease in C_I and an absolute increase in C_F.

To gain further insight into the variation of the internal conversion, the baroclinic conversion, which evolves roughly similarly to C_I (not shown), is studied and for this purpose is decomposed into the configuration term and the baroclinicity (section 3). In J_{50}, there is a good temporal correlation between the baroclinic conversion and the baroclinicity, which suggests an almost constant configuration term. In particular, when the perturbation crosses the jet, its configuration is as favorable to an efficient extraction of energy from the environment as initially. In J_{30}, things are very different. The baroclinic conversion is maximum 36 h before the jet crossing and then decreases strongly, which means that the perturbation configuration becomes less favorable to efficient baroclinic interaction when baroclinicity is maximum. This is tightly linked with the fact, pointed out in section 4, that a strong anticyclonic horizontal shear enables a good configuration between the upper and lower anomalies.

To sum up, the energy evolutions in the two simulations differ markedly, essentially because of two factors. First, the higher background gradient of PV in J_{50} induces an unequivocal crossing of the jet, whereas this crossing is less clear in J_{30}. Second, the stronger horizontal shear of J_{50} maintains a better configuration of the upper and lower anomalies than in J_{30}, where they tend to turn around one another. These factors lead to an energy budget such that in J_{30}, the rate of change of kinetic energy reaches a single maximum before the crossing of the jet, whereas in J_{50} a clear regeneration and a speeding up of the growth can be observed subsequently to the jet crossing.

Three other simulations in J_{50} starting with different initial conditions are now studied. Figure 15 shows that in the four simulations (control plus these three modified runs), the same kind of evolution is found. A systematic change of slope can be seen: a sudden stronger deepening of the streamfunction and a temporary intensification of the vorticity growth (not shown) occur following the jet crossing. In the three modified runs, the anomalies are more strongly stretched horizontally than in the control run and are always within the jet dilatation axis (not shown). Before the jet crossing, C_K is all the stronger when the structure is stretched horizontally and is thus stronger in the modified experiments. Nevertheless, this term is always of secondary importance with respect to the other conversion terms. This fact is at sharp variance with the diagnosis made on real cases such as IOP 17 (Rivière and Joly 2006a). In the latter case, C_K as well as C_F and C_I have been shown to be the major contributors to the energy regeneration subsequent to the jet crossing. It has been checked that in J_{30}, a change of slope in the streamfunction variation does

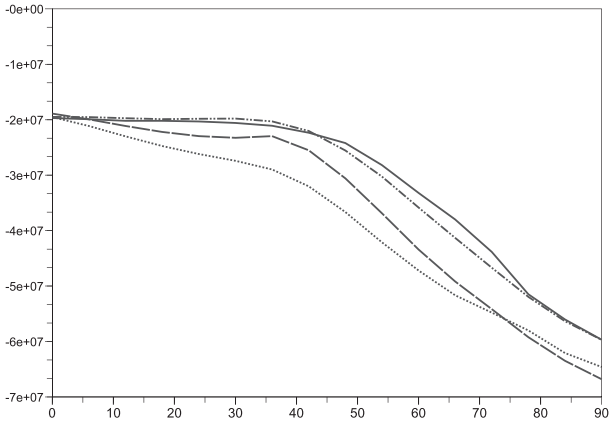

FIG. 15. Time variation up to $t = 78$ h of the streamfunction minimum for different initial conditions. Same initial conditions as previously (dotted line), without an initial upper layer anomaly (mixed dashed–dotted line); both anomalies are stretched within the jet dilatation axis (i.e., stretched at an angle of +45° with respect to the x axis) (solid line) and the anomaly size increased by 1.5 (dashed line).

not generally occur except with very specific initial conditions. Globally, these results suggest that a complex life cycle with, in particular, a strong change in the growth of the perturbation is favored in jets that have strong barotropic components, all other things being equal. These different evolutions sometimes lead to a stronger growth in J_{50} than in J_{30} (experiments with unmodified initial conditions and enlarged initial anomalies), and this fact cannot be linked directly with barotropic conversion but rather with a better vertical configuration of the upper and lower anomalies.

c. Comparison with linear dynamics

Finally, linear simulations with the same basic states J_{30} and J_{50} and unmodified anomalies were carried out to highlight the impact of nonlinearities on the perturbation evolution.

In the linear simulation with the jet J_{50} (Fig. 16), the vortices stay at roughly the same latitude or come closer to the jet axis but do not cross it. They are so strongly stretched horizontally that even if the growth of the vorticity maximum is close to that obtained in the full nonlinear simulation, the streamfunction deepening stops after 40 h (Fig. 17a). At the end of the simulation, the perturbation streamfunction minimum is only 1.4 times lower than initially, whereas it deepens by a factor of approximately 2.6 in the nonlinear simulation. This difference arises mainly from the fact that the jet crossing only occurs in the nonlinear simulation and thus the subsequent acceleration of the deepening only happens in this case.

In J_{30}, contrary to the case just mentioned, the linear evolution induces a much stronger deepening of streamfunction than the nonlinear one (Fig. 17b). This arises because in the nonlinear simulation the two anomalies turn around each other and are less favorably vertically tilted for baroclinic interaction than in the linear simulation.

Note that J_{30} is much more linearly unstable than J_{50}. The addition of a barotropic component tends to cancel the linear instability, as shown by James (1987). It is interesting to note that for the specific nonlinear simulations shown here, such a difference does not exist and, in some cases, J_{50} is even more favorable to rapid cyclone growth during jet-crossing transitions.

6. Conclusions

The evolution of two initially circular cyclonic vortices, located one in the upper and one in the lower layer of a two-layer model and favorably configured for baroclinic

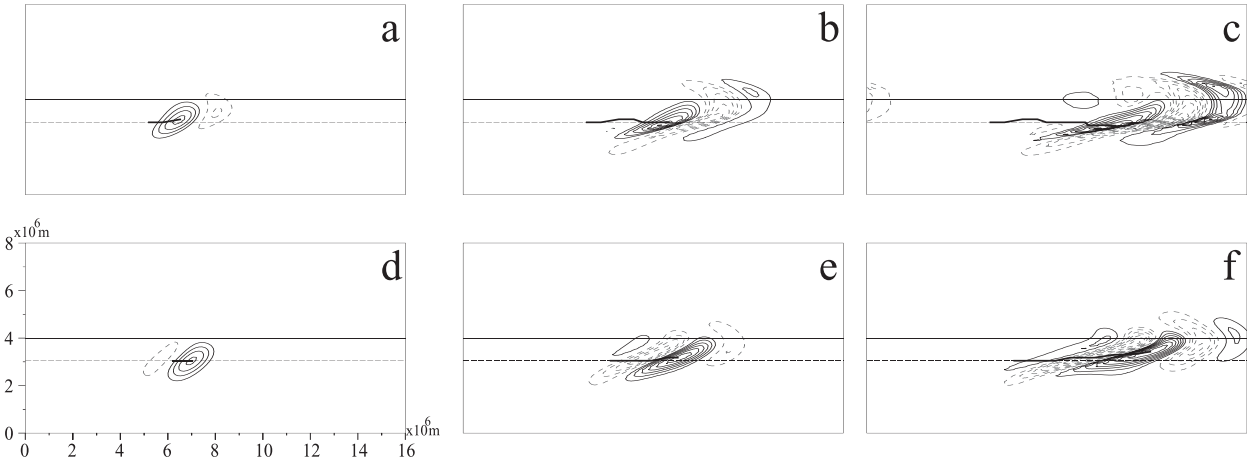

FIG. 16. As in Fig. 11, but for the linear simulation.

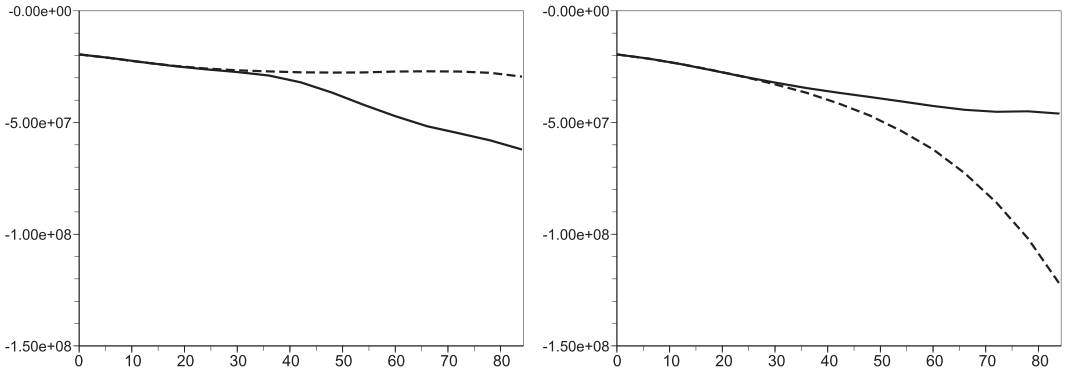

FIG. 17. 84-h evolution of the streamfunction minimum in (left) J_{50} and (right) J_{30} in the two-layer baroclinic simulation. Solid and dashed lines correspond to nonlinear and linear simulations, respectively.

interaction, has been first studied in the presence of zonally uniform vertical and horizontal shears.

Two nonlinear effects have been underlined, one acting on the shape and deepening of the lower anomaly and the other on its latitudinal shift. It has been shown that its horizontal shape depends strongly on the sign of the horizontal background shear: if the cyclonic vortex is embedded in an anticyclonic shear, it is stretched strongly, which leads to a loss of kinetic energy through barotropic effects, whereas in a cyclonic shear it remains more or less isotropic and the barotropic conversion rates are quite weak. However, an anticyclonic shear favors the maintenance of a favorable vertical tilt that induces a long-lasting positive baroclinic interaction between the anomalies, whereas the upper and lower structures in a cyclonic shear turn around each other and the initially favorable westward tilt with height is rapidly lost. As for the second nonlinear effect, the trajectory of the surface cyclone has been shown to depend strongly on the value of β, which is precisely the vertically averaged meridional PV gradient in uniform background shear flows. The latitudinal shift is all the faster when the meridional component of the PV gradient reaches large positive values.

In a confined westerly jet, it has been shown that surface cyclones initially located south of the jet move poleward because of the poleward orientation of the vertically averaged PV gradient. A crossing of the jet axis is possible if the jet has a strong enough barotropic component since it increases the vertically averaged PV gradient, which plays the role of an effective β. More precisely, if the environment has realistic characteristics, the poleward variation of PV is positive in the upper layer and negative in the lower layer. If the tropopause and surface anomalies are linked with each other, there is a necessary compensation of the local action of the PV gradient. This is done through the nonlinear stretching term, which results in a shift that is consistent with the vertically averaged PV gradient. When a crossing is obtained, the anomaly becomes almost isotropic and an energy regeneration is observed. A kinetic energy budget shows that this regeneration is essentially due to a favored combination of the internal conversion rate and the vertical geopotential fluxes and may in some cases be slightly reinforced by barotropic interaction. The experiments shown here and all the complementary ones performed by the authors (not shown) tend to show that this crossing and the subsequent shape and energy disparities cannot be accounted for by linear diagnosis and in particular that the predictability of these even very simple jets cannot be studied through the analysis of singular vectors (Plu and Arbogast 2005).

The present results provide indications on the mechanisms leading to the well-known observational finding that mature midlatitude synoptic cyclonic perturbations shift to the left of the jet (e.g., Wallace et al. 1988). The mechanisms highlighted here may be helpful for the analysis of complex life cycles during which an energy regeneration occurs subsequent to a jet crossing. It suggests that a deep cyclone situated on the southern side of a zonal baroclinic jet that is sufficiently meridionally confined will shift to the north, can cross the jet, and may have a complex life cycle with regeneration on the northern side of the jet. Nevertheless, a number of characteristics of some observed intense storms have not been reproduced. In particular, the barotropic conversion in the energy budget is much stronger in real cases such as the depression observed during IOP 17 of the FASTEX campaign (Rivière and Joly 2006a). Other studies in more complex flows, notably in the presence of zonally nonuniform jets, should help to fill this gap.

Acknowledgments. The authors thank Alain Joly for initiating this study, Guillaume Lapeyre for fruitful scientific discussions, and Susan Becker for her careful proofreading.

APPENDIX

Vertical Velocity

The vertical velocity w_m is obtained by solving the following linear equation:

$$(\Delta - 2\lambda^{-2})\left(-\frac{f_0 w_m}{H}\right) = \lambda^{-2}\nabla \cdot \mathbf{Q}. \tag{A1}$$

A distinction between the linear and the nonlinear vertical velocity can be achieved by separating the $\mathbf{Q}$ vector into the sum $\mathbf{Q_1} + \mathbf{Q_2}$, where

$$\mathbf{Q}_1 = \begin{bmatrix} \dfrac{\partial \mathbf{u}'_\mathbf{m}}{\partial x}\nabla(\overline{\psi_\mathbf{u}} - \overline{\psi_\mathbf{l}}) + \dfrac{\partial \overline{\mathbf{u}_\mathbf{m}}}{\partial x}\nabla(\psi'_\mathbf{u} - \psi'_\mathbf{l}) \\ \dfrac{\partial \mathbf{u}'_\mathbf{m}}{\partial y}\nabla(\overline{\psi_\mathbf{u}} - \overline{\psi_\mathbf{l}}) + \dfrac{\partial \overline{\mathbf{u}_\mathbf{m}}}{\partial y}\nabla(\psi'_\mathbf{u} - \psi'_\mathbf{l}) \end{bmatrix} \quad \text{and}$$

$$\mathbf{Q}_2 = \begin{bmatrix} \dfrac{\partial \mathbf{u}'_\mathbf{m}}{\partial x}\nabla(\psi'_\mathbf{u} - \psi'_\mathbf{l}) \\ \dfrac{\partial \mathbf{u}'_\mathbf{m}}{\partial y}\nabla(\psi'_\mathbf{u} - \psi'_\mathbf{l}) \end{bmatrix}, \tag{A2}$$

with $\mathbf{u_m} = \frac{1}{2}(\mathbf{u_u} + \mathbf{u_l})$. The term $(f_0 w_m/\mathrm{H})$ resulting from Eq. (A1) with only $\mathbf{Q_1}$ on the right-hand side is the linear vertical stretching term, and the one with $\mathbf{Q_2}$ is the nonlinear stretching term.

REFERENCES

Adem, J., 1956: A series solution for the barotropic vorticity equation and its application in the study of atmospheric vortices. *Tellus,* **8,** 364–372.

Alpert, P., 1989: Comments on "Relationship between cyclone tracks, anticyclone tracks, and baroclinic waveguides." *J. Atmos. Sci.,* **46,** 3505–3507.

Anthes, R., 1982: *Tropical Cyclones: Their Evolution, Structure and Effects. Meteor. Monogr.,* No. 41, Amer. Meteor. Soc., 208 pp.

Baehr, C., B. Pouponneau, F. Ayrault, and A. Joly, 1999: Dynamical characterization of the FASTEX cyclogenesis cases. *Quart. J. Roy. Meteor. Soc.,* **125,** 3469–3494.

Cai, M., and M. Mak, 1990: On the basic dynamics of regional cyclogenesis. *J. Atmos. Sci.,* **47,** 1417–1442.

Davies, H. C., C. Schär, and H. Wernli, 1991: The palette of fronts and cyclones within a baroclinic wave development. *J. Atmos. Sci.,* **48,** 1666–1689.

Dritschel, D., 1998: On the persistence of non-axisymmetric vortices in inviscid two-dimensional flows. *J. Fluid Mech.,* **371,** 141–155.

Holland, G., 1983: Tropical cyclone motion: Environmental interaction plus a beta effect. *J. Atmos. Sci.,* **40,** 328–342.

Hoskins, B. J., and N. V. West, 1979: Baroclinic waves and frontogenesis. Part II: Uniform potential vorticity jet flows—Cold and warm fronts. *J. Atmos. Sci.,* **36,** 1663–1680.

James, I., 1987: Suppression of baroclinic instability in horizontally sheared flows. *J. Atmos. Sci.,* **44,** 3710–3720.

Kida, S., 1981: Motion of an elliptic vortex in a uniform shear flow. *J. Phys. Soc. Japan,* **50,** 3517–3520.

Legras, B., and D. Dritschel, 1993: Vortex stripping and the generation of high vorticity gradients in two-dimensional flows. *Appl. Sci. Res.,* **51,** 445–455.

Madala, R., and A. Piacsek, 1975: Numerical simulation of asymmetric hurricane on a beta-plane with vertical shear. *Tellus,* **27,** 453–468.

Marcus, P., T. Kundu, and C. Lee, 2000: Vortex dynamics and zonal flows. *Phys. Plasmas,* **7,** 1630–1640.

McWilliams, J., and G. Flierl, 1979: On the evolution of isolated nonlinear vortices. *J. Phys. Oceanogr.,* **9,** 1155–1182.

Morel, Y., and J. McWilliams, 1997: Evolution of isolated interior vortices in the ocean. *J. Phys. Oceanogr.,* **27,** 727–748.

Orlanski, I., and J. Sheldon, 1995: Stages in the energetics of baroclinic systems. *Tellus,* **47A,** 605–628.

Phillips, N., 1951: A simple three-dimensional model for the study of large-scale extratropical flow patterns. *J. Meteor.,* **8,** 381–394.

Plu, M., and P. Arbogast, 2005: A cyclogenesis evolving into two distinct scenarios and its implications for short-term ensemble forecasting. *Mon. Wea. Rev.,* **133,** 2016–2029.

Rivière, G., 2008: Barotropic regeneration of upper-level synoptic disturbances in different configurations of the zonal weather regime. *J. Atmos. Sci.,* **65,** 3159–3178.

——, and A. Joly, 2006a: Role of the low-frequency deformation field on the explosive growth of extratropical cyclones at the jet exit. Part I: Barotropic critical region. *J. Atmos. Sci.,* **63,** 1965–1981.

——, and ——, 2006b: Role of the low-frequency deformation field on the explosive growth of extratropical cyclones at the jet exit. Part II: Baroclinic critical region. *J. Atmos. Sci.,* **63,** 1982–1995.

Rossby, C., 1948: On displacements and intensity changes of atmospheric vortices. *J. Mar. Res.,* **7,** 175–187.

Schär, C., and H. Wernli, 1993: Structure and evolution of an isolated semi-geostrophic cyclone. *Quart. J. Roy. Meteor. Soc.,* **119,** 57–90.

Shapiro, L., 1992: Hurricane vortex motion and evolution in a three-layer model. *J. Atmos. Sci.,* **49,** 140–154.

Simmons, A. J., and B. J. Hoskins, 1978: The life cycles of some nonlinear baroclinic waves. *J. Atmos. Sci.,* **35,** 414–432.

Smith, R., and W. Ulrich, 1990: An analytical theory of tropical cyclone motion using a barotropic model. *J. Atmos. Sci.,* **47,** 1973–1986.

Sutyrin, G., and Y. Morel, 1997: Intense vortex motion in a stratified fluid on the beta-plane: An analytical theory and its validation. *J. Fluid Mech.,* **336,** 203–220.

Takayabu, I., 1991: Coupling development: An efficient mechanism for the development of extratropical cyclones. *J. Meteor. Soc. Japan,* **69,** 609–628.

Uccelini, L. W., 1990: Processes contributing to the rapid development of extratropical cyclones. *Extratropical Cyclones: The Erik Palmén Memorial Volume,* C. W. Newton and E. O. Holopainen, Eds., Amer. Meteor. Soc., 81–105.

Wallace, J., G.-H. Lim, and M. Blackmon, 1988: Relationship between cyclone tracks, anticyclone tracks and baroclinic waveguides. *J. Atmos. Sci.,* **45,** 439–462.

Willoughby, H., 1988: Linear motion of a shallow-water, barotropic vortex. *J. Atmos. Sci.,* **45,** 1906–1928.